# Magnetic Shield Design for Double-D Coil-Based Wireless Charging System

Mostak Mohammad, *Senior Member, IEEE,* Omer C. Onar, *Senior Member, IEEE,* Veda P. Galigekere, *Senior Member, IEEE,* Gui-Jia Su, *Senior Member, IEEE,* and Jonathan Wilkins

***Abstract*—In this study, magnetic field emission (MFE) of the high-power double-D (DD) coil-based wireless charging system is investigated and a shielding technique is proposed. The MFE pattern produced by the DD coils is significantly different from the MFE of the unipolar (e.g., circular, square, or rectangular) coils, and the traditional aluminum shield does not suppress the MFE from the DD coils. This study shows that a conventional aluminum shield increases the MFE, and a magnetic shield effectively suppresses the MFE of the DD coils. Therefore, a magnetic shield consisting of high-permeability magnetic material, such as ferrites, nanocrystalline, etc., is proposed for the DD pads. The shielding effectiveness of the proposed shield is evaluated through finite element analysis and verified through experiments. An 11 kW DD coil-based wireless charging system was used to test the proposed shielding technique. The experimental results show that a traditional aluminum shield increased the MFE by 29.8%, and the proposed magnetic shield suppressed the MFE by 50.5%.**

***Index Terms*—Inductive charging, wireless power transfer, electric vehicle, leakage field, electromagnetic field emissions, shielding effectiveness.**

## I. Introduction

WIRELESS charging system (WCS) is one of the most promising technologies being investigated to enhance the convenience of charging electric vehicles (EVs) [1]–[6]. Improvement in the efficiency and power density of WCSs along with the rapid growth of the EV market—which benefits from fast and convenient charging—have resulted in significant academic and industrial research attention on developing WCSs for high-power EV charging [7], [8]. However, for high-power EV charging, the WCSs are highly prone to produce a significant level of electromagnetic field (EMF) emissions, causing serious health and safety concerns, if the couplers and shields are not designed properly [9]–[14].

The power level of WCSs in EV applications ranges from a few hundred watts for small golf-carts, 3 to 20 kW for light-duty passenger vehicles, and greater than 50 kW for electric buses [15], [16]. A typical WCS for light-duty vehicles is depicted in Fig. 1. Depending on the vehicle type, the airgap between the transmitter and receiver pads ranges between 10 to 25 cm.

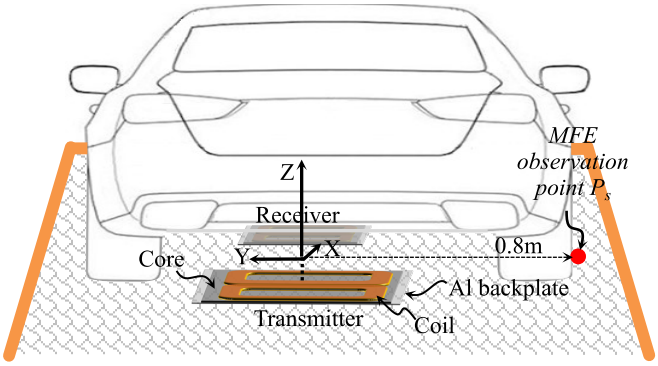


Fig. 1. The basic components of an EV WCS showing typical locations and orientations of the bipolar transmitter and receiver pad.

The WCSs in EV applications may produce high EMF emissions both inside and around the vehicle because a significant amount of power is transferred over a large airgap. Field emissions are a serious safety concern and limiting them below safety levels of international guidelines is one of the main engineering challenges for high-power WCSs [16], [17]. In addition to causing health issues, field emissions may also interfere with other vehicle-side electronic systems such as keyless entry and remote start systems, tire pressure sensors, and vehicle infotainment systems. In the case of connected and automated vehicles, other controls, communications, and sensing systems may also be impacted. To address these concerns, WCSs should meet the limits outlined by international regulations. There are several regulatory limits on low-frequency (<1 MHz) EMF emissions [18]. For EMF emissions testing, the Society of Automotive Engineers (SAE) standard J2954 is following the guidelines of the International Commission of Non-Ionized Radiation Protection (ICNIRP) [19], [20]. The MFE is the dominant EMF emission for an inductive WCS. According to the ICNIRP 2010 guidelines, the magnetic field limit for the 3 kHz to 10 MHz frequency range is 27 $\mu T_{RMS}$ for general-public exposure and 15 $\mu T_{RMS}$ in areas where body-implanted pacemakers are a concern.

In literature, different shield designs have been investigated to suppress the MFE of the WCS [16], [21]–[26]. To limit the MFE below the ICNIRP limits, SAE has recommended a large (800 × 800) mm aluminum shield above the receiver

M. Mohammad, O. C. Onar, V. P. Galigekere, and Gui-Jia Su are with the Building and Transportation Science Division of Oak Ridge National Laboratory, Oak Ridge, TN, 37830 USA

Corresponding author: Mostak Mohammad, R&D Staff Member, Oak Ridge National Laboratory, 1 Bethel Valley Road, P.O. Box 2008, MS-6472, Oak Ridge, TN 37830, email: mostak@ieee.org, phone: 1-330-687-8337.

This manuscript has been authored by UT-Battelle, LLC, under contract DE-AC05-00OR22725 with the US Department of Energy (DOE). The US government retains and the publisher, by accepting the article for publication, acknowledges that the US government retains a nonexclusive, paid-up, irrevocable, worldwide license to publish or reproduce the published form of this manuscript, or allow others to do so, for US government purposes. DOE will provide public access to these results of federally sponsored research in accordance with the DOE Public Access Plan (https://energy.gov/downloads/doe-public-access-plan).

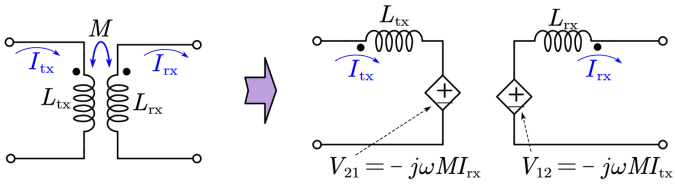


Fig. 2. Schematic diagram of the coupled coils of a wireless charging system.

pad [19]. The undercarriages of the battery EVs are flat, metallic, and ferrous (in some cases), which also act as a lossy conductive shield. Both the large aluminum shield and the EV undercarriage effectively suppress the MFE of the unipolar (e.g., circular, rectangular) charging pads [27]. However, the conductive aluminum shield is not effective for DD charging pads [14]. Therefore, the MFE from the DD charging pads mostly exceed the ICNIPR limit of 27 $\mu T_{\rm RMS}$ even at 11 kW power levels [28], especially under misaligned conditions.

Different active and passive shielding methods have been proposed for WCSs in the literature. Most of the shield designs are investigated for unipolar circular and rectangular pads [15], [16], [27], [29]–[31]. However, the magnetic shield (MS) has been limitedly investigated for the DD pads. Lin et al. [32] investigated the MFE of a DD coil at a power of a few kilowatts. However, the suppression method of those fields from high-power DD pads has not been studied. In another work from Lin et al. [33], a partial ferrite extension showed a 46% reduction of the MFE of the DD pads. Song et al. [34] showed that a certain extension of the ferrite core reduces the MFE of a 6.6 kW DD coil-based WCS pad for a limited power application. Although those works indicate that a high-permeability MS is promising for the DD pads, they do not show a shield design that can be generalized and applied for up to several hundred kilowatts of power. In [9], the authors designed a specific MS for a 100 kW DD coil-based WCS, which reduces the MFE below the ICNIRP limits using the least amount of additional ferrite. In [35] and [36], the authors have proposed a magnetic shield to suppress the MFE from interoperating and polyphase WCSs. In this paper, a detailed characterization of the MFE from DD pads is investigated, and a generalized shield design is proposed, which can be extended for extremely high-power DD coil-based WCSs.

In Sections II and III, the characteristics of the MFE of DD coils are studied. In Section IV, the design and optimization of the proposed MS are presented. In Section V, experimental results are given comparing the effectiveness of the proposed shield and the traditional aluminum shield for an 11 kW mismatched (different sizes of transmitter and receiver pads) DD coil-based WCS.

## II. Analytical Properties of MFE

The currents through the transmitter and receiver coils are the primary source of MFE. The total ampere-turns in the transmitter and receiver coils are determined by the operating frequency, coupling factor, and the required output power. A schematic diagram of the coupled circuit of a WCS is shown in Fig. 2.

Power flow from the primary coil to the secondary coil can be given as [37]

$$P = \omega M I_{tx} I_{rx}^* = 2\pi f k \sqrt{L_{tx} L_{rx}} I_{tx} I_{rx}^* \tag{1}$$

where $I_{tx}$ and $I_{rx}$ are the transmitter and receiver coil currents, $f$ is the operating frequency, $L_{tx}$ and $L_{rx}$ are the self-inductances, and $k$ is the coupling coefficient. The inductance of the coils can be expressed in terms of the number of turns and average inductance per turn as

$$\begin{aligned} L_{tx} &= N_{tx}^2 \hat{L}_{tx} \\ L_{rx} &= N_{rx}^2 \hat{L}_{rx} \end{aligned} \tag{2}$$

where $\hat{L}_{tx}$ and $\hat{L}_{rx}$ are the average inductance-per-turn of the transmitter and receiver coils. Using the expressions of Eq. (2), Eq. (1) can be further expanded to

$$P = 2\pi f k (N_{tx} I_{tx})(N_{rx} I_{rx}^*) \sqrt{\hat{L}_{tx} \hat{L}_{rx}} \tag{3}$$

The equations show that the number of ampere-turns in the transmitter and receiver at a certain power is determined by the coupling coefficient, frequency, and size of the coils, which determine the $\hat{L}_{tx}$ and $\hat{L}_{rx}$. The geometric parameters $k$, $\hat{L}_{tx}$, and $\hat{L}_{rx}$ depend on the size, shape, and topology of the pad and can be assumed to be independent of the number of turns. Equation (2) shows that for a given power level, the ampere-turns of the coils (a key factor for MFE) are determined by the size of the coils and the operating frequency. For a fixed airgap, size, and alignment of the charging pads, $k$, $\hat{L}_{tx}$, and $\hat{L}_{rx}$ are constant and do not depend on the number of turns. Hence, according to (3), $(N_{tx} I_{tx} N_{rx} I_{rx})$ is also constant for a fixed pad size, alignment, airgap, and output power.

The ratio between the primary and secondary ampere-turns can be given as $r_{NI} = (N_{tx} I_{tx})/(N_{rx} I_{rx})$. A WCS can be designed and operated with different $r_{NI}$ for a certain power, equivalently, with different voltage-current loading in the primary and secondary coils. These variations of $r_{NI}$ significantly impact the MFE of the system. Therefore, the ratio $r_{NI}$ needs to be optimized during the design stage, and during the operation under different misalignment conditions. For a geometrically matched system with identically sized transmitter and receiver pads, the MFE per unit ampere-turns from the transmitter and receiver pads are the same [38]. Hence, the minimum MFE is achieved when $r_{NI} \approx 1$. On the other hand, for the commonly used mismatched systems, the transmitter is considerably larger than the receiver. In such systems, the MFE per unit ampere-turns from the transmitter are much higher than the receiver. Hence, it is essential to optimize the $r_{NI}$ to minimize the unshielded MFE and identify the relative MFE from each pad and design the shield accordingly. Optimization of $r_{NI}$ further depends on the input-output voltages and degree of freedom in the selected compensation topology, which is beyond the scope of this work. This paper primarily focuses on the design and optimization of the shield for a fixed $r_{NI}$.

### A. Separating MFE due to the Transmitter and Receiver Pads

The flux density at any point is the vector sum of the flux densities due to the transmitter and receiver ampere-turns, which can be expressed as

$$\mathbf{B} = \mathbf{B}_{tx} + \mathbf{B}_{rx} \tag{4}$$

where $\mathbf{B}_{tx}$ is the flux density generated by the transmitter current $I_{tx}$, and $\mathbf{B}_{rx}$ is the flux density generated by the receiver current $I_{rx}$. Moreover, the MFE is the vector sum of the MFE generated by the transmitter and receiver coils. The MFE contribution from each coil depends on their ampere-turns, their sizes, and positions relative to the observation point. The relation between the coil size and MFE is complicated to express analytically for a coil with ferrite and aluminum backplate. Commonly, a finite element analysis (FEA) tool is used to evaluate these flux-density distributions around the 2D or 3D models of the coils, where the ampere-turns are provided as the coil-excitation. The flux density is proportional to the ampere-turns of the coils, which can be expressed as:

$$\begin{aligned} B_{tx} &\propto N_{tx} I_{tx} \\ B_{rx} &\propto N_{rx} I_{rx} \end{aligned} \tag{5}$$

Therefore, once the MFE is simulated through FEA for per unit ampere-turns for the transmitter and receiver pads, the final MFE can be calculated using (4). This is a frequently used approach in investigating the MFE of a WCS. However, this approach is limited to a specific size, geometry, and coil position. Therefore, this approach is challenging to understand the individual contribution of MFE, $B_{tx}$ and $B_{rx}$, during a geometric design and optimization process, and also during the testing of a WCS.

A supplementary approach is to segregate MFE based on the current phase angle, which is only applicable when the $I_{tx}$ and $I_{rx}$ are highly sinusoidal and orthogonal in phase. In such cases, the MFE of the transmitter and receiver are also orthogonal in phase. This property can be utilized to identify the relative contribution to MFE from the individual pads and to design the shield accordingly.

The primary and secondary coil currents are highly sinusoidal in an inductive WCS due to the band-pass filter characteristics of the resonant tuning or compensation networks. Hence, the first harmonic approximation can be adopted for the analytical modeling. Moreover, the coil currents are approximately 90° phase apart at the resonant point, which can be expressed in complex form as

$$\begin{aligned} I_{tx} &= \hat{I}_{tx} + j0 \\ I_{rx} &= 0 + j\hat{I}_{rx} \end{aligned} \tag{6}$$

where $\hat{I}_{tx}$ and $\hat{I}_{rx}$ are the peak values of $I_{tx}$ and $I_{rx}$. Equations (5) and (6) indicate that the real and imaginary parts of the flux density are generated by the transmitter and receiver currents, respectively, which can be expressed as

$$\begin{aligned} B_{tx} &= \text{real}(B) \\ B_{rx} &= \text{img}(B) \end{aligned} \tag{7}$$

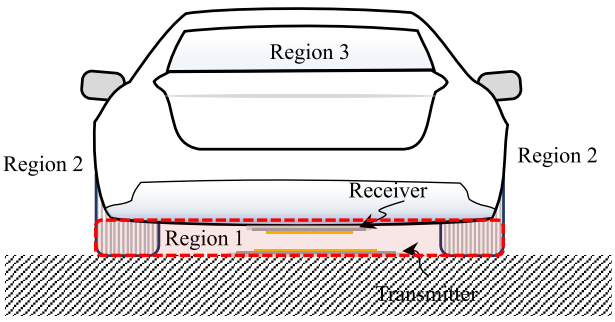


Fig. 3. Three regions inside and outside an EV with different EMF limits.

The vector components of the time-varying leakage flux at the observation point can also be represented by its vector components as

$$\mathbf{B} = \hat{x}B_x + \hat{y}B_y + \hat{z}B_z \tag{8}$$

where $B_x, B_y$, and $B_z$ are the $x$, $y$, and $z$ directional components of the flux density, and $\hat{x}$, $\hat{y}$, and $\hat{z}$ are the unit vectors associated with the Cartesian coordinate system. Each vector component of the AC magnetic field can be expressed in complex form as

$$\begin{aligned} B_x &= B_{x-\text{real}} + jB_{x-\text{img}} \\ B_y &= B_{y-\text{real}} + jB_{y-\text{img}} \\ B_z &= B_{z-\text{real}} + jB_{z-\text{img}} \end{aligned} \tag{9}$$

where the subscript 'real' indicates the real and 'img' indicates the imaginary components of the complex representation of the time-varying sinusoidal waveform.

From Eqs. (7) and (9), the vector component of the MFE generated by the transmitter and receiver coil can be separated as:

$$\begin{aligned} \mathbf{B}_{tx} &= \text{real}(\mathbf{B}) = \hat{x}B_{x-\text{real}} + \hat{y}B_{y-\text{real}} + \hat{z}B_{z-\text{real}} \\ \mathbf{B}_{rx} &= \text{img}(\mathbf{B}) = \hat{x}B_{x-\text{img}} + \hat{y}B_{y-\text{img}} + \hat{z}B_{z-\text{img}} \end{aligned} \tag{10}$$

As the MFE from the transmitter and receiver pads is separated by Eq. (10), the shielding requirement for the transmitter and the receiver pad becomes more specific and can be clearly identified.

### B. Tx-Rx Orientation and Observation Points

In the SAE International J2954 standard, the regions around and inside the vehicle have been segregated into three regions, as shown in Fig. 3: first, Region 1, which is under the vehicle and not subject to ICNIRP limit; second, Region 2, which is on the sides of the vehicle and subject to ICNIRP limits of the public region; third, Region 3, which is inside the vehicle, where the limit is 15 $\mu\text{T}_{\text{RMS}}$.

Following the J2954 recommendation, the distance of the test plane is set at 800 mm away from the center of the receiver, in Region 2, where the public exposure limit of the MFE is 27 $\mu\text{T}_{\text{RMS}}$ [19]. Assuming the origin of the axis system on the center of the transmitter pad, two observation points were selected along the x- and y-axis at 800 mm away, which are denoted as $\text{P}_\text{F}$ and $\text{P}_\text{S}$, as shown in Fig. 4. Moreover,

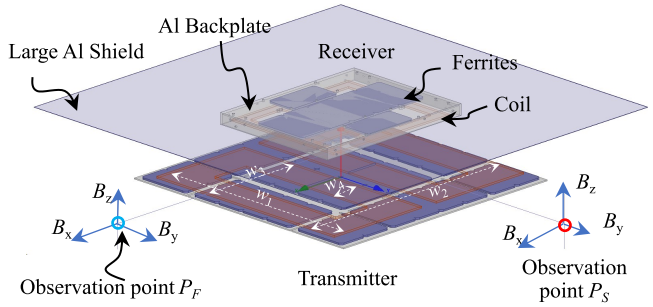


Fig. 4. FEA model of the 11 kW DD-coil-based WCS and the observation points, where the MFE were evaluated through this study.

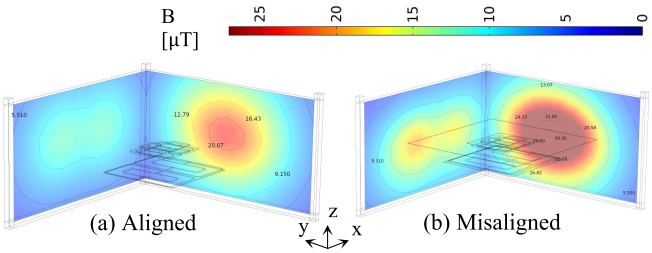


Fig. 5. MFE under alignment and misalignment ($\Delta x$ = -100 mm, $\Delta y$ = -70 mm) conditions for the coil currents that are given in Table I.

the ZX-plane through the $P_S$ point and YZ-plane through the $P_F$ point are referred to as S-plane (side) and F-plane (front), respectively. The vehicle undercarriages of EVs are mostly made of high-strength steel and aluminum alloy, which also act as a conductive shield for the magnetic fields. To mimic EV shielding, an 1 m × 1 m × 0.7 mm large aluminum plate was placed above the receiver for both simulation and testing.

## III. Finite Element Analysis of MFE

The FEA model of the 11 kW system is shown in Fig. 4, and the system parameters of the test WCS prototype are given in Table I. The inductances of the coupled coils were measured under the aligned condition, and the airgap was measured between the transmitter coil to the receiver coil surfaces. The FEA simulation was performed in COMSOL Multiphysics, and the 'infinite domain' approximation was applied outside the simulation region (1.6 m × 1.6 m × 1 m) to simulate the MFE. Two main observation points, $P_S$ and $P_F$ indicate the position at the side and front of the vehicle, respectively. Figure 5 shows the FEA results of the MFE at the aligned and misaligned positions of the vehicle. Both the primary and secondary currents were equally increased to maintain the same power transfer with reduced coupling under misalignment. The results show that the MFE at the front of the vehicle was nearly twice the MFE at the sides. Moreover, the maximum MFE was 20.07 $\mu T_{RMS}$ for the aligned position and 39.36 $\mu T_{RMS}$ for the misaligned position. The results indicate that the MFE exceeded the ICNIRP limits, and a more effective shield is essential to safely run the system for all alignment conditions.

Table I
System Parameters of an 11 kW WCS

| Parameter | Value |
|---|---|
| Power rating | 11 kW |
| Nominal DC input voltage, $V_{dc}$ | 370 V |
| Nominal DC output voltage, $V_o$ | 350 V |
| Current in coils, $I_{tx}$, $I_{rx}$ | 42 A, 35 A |
| Number of turns, $N_{tx}$, $N_{rx}$ | 6.25, 8.2 |
| Inductance, $L_{tx}$, $L_{rx}$ | 73 μH, 84 μH |
| Transmitter size | 650 × 650 mm |
| Transmitter $w_1$, $w_2$, $w_3$, $w_4$ | 644, 644, 317, 97 mm |
| Receiver size | 350 × 350 mm |
| Coupling coefficient, $k$ | 0.175 |
| Airgap, $d$ | 150 mm |

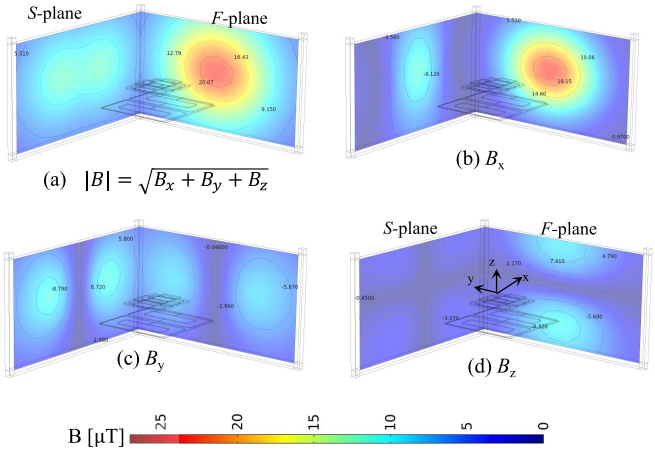


Fig. 6. Comparison of $B_x$, $B_y$, and $B_z$ of MFE of the unshielded bipolar coil-based 11 kW WCS.

### A. Vector Analysis of Leakage Magnetic Field

The MFEs and their vector components $B_x$, $B_y$, and $B_z$ on the S-plane and F-plane are shown in Fig. 6. The results show that $B_x$ and $B_y$ are the two most dominant components in the regions between the pad. Because of the horizontally dominant MFE components, an aluminum shield is almost ineffective for the DD pads; instead, a high-permeability MS is a promising technique for such field orientation. The high-permeability path of an MS provides a low-reluctance route for such stray magnetic fields and for reducing the MFE. The vector components of the MFE at $P_S$ and $P_F$ are shown in Fig. 7, which indicates that the DD pad had significantly larger $B_x$ components than $B_y$ and $B_z$, at both $P_F$ and $P_S$. These findings of the vector components of the magnetic field significantly influenced the design of an effective MS.

### B. MFE from the Transmitter and Receiver Pads

As described in Section II, the real and imaginary components of the complex representation of the MFE show the contribution of the transmitter and receiver pads. The real and imaginary MEF components at $P_S$ and $P_F$ are given in Table II and shown in Fig. 8. The figure shows that at both points, more than 95% of the total MFE was generated by the transmitter


(a) MFE at $P_S$


(b) MFE at $P_F$

Fig. 7. Vector components of the MFE of the 11 kW bipolar coil based WCS at the observation points (a) $P_S$ and (b) $P_F$.

Table II
VECTOR AND PHASOR COMPONENTS OF THE PEAK MFE (μT)

| | $B$ at $P_F$ | | $B$ at $P_S$ | |
|---|---|---|---|---|
| | $B_{tx}$ | $B_{rx}$ | $B_{tx}$ | $B_{rx}$ |
| $B_x$ | +33.6 | -5.10i | -14.97 | +2.04i |
| $B_y$ | -0.01 | +0.01i | -0.01 | +0.001i |
| $B_z$ | -2.90 | +1.00i | +0.001 | +0.001i |
| $B_{peak}$ | +33.7 | -5.20i | +14.97 | +2.04i |

pad. Since the transmitter is found to have a significantly larger contribution to the MFE, the shield design needs a greater emphasis on the transmitter pad than the receiver pad.

### *C. Comparison of Shielding Effectiveness (SE) of Different Shields for Bipolar Pads*

Each DD pad has a clockwise and a counterclockwise winding direction, which are series-connected; therefore, those windings carry the same current in opposite directions. The $z$-components of the MFE from those two windings cancel each other to a great extent, resulting in a small $B_z$. Moreover, the flux linking between the two windings generates a horizontally aligned flux emission in the air, which contributes to the MFE. The orientation of the flux density distribution from a DD coil is illustrated in Fig. 9.

For clarity of comparison, the SE at any point is represented in terms of the relative flux density as [9]

$$_{\mathrm{sh}-1}\mathrm{SH}_{\mathrm{sh}-2} = \frac{B_{sh-2}}{B_{sh-1}} \tag{11}$$

where $_{\mathrm{sh}-1}\mathrm{SE}_{\mathrm{sh}-2}$ is the SE of shield sh-2 with respect to a reference shield sh-1, $B_{sh-1}$ is the magnetic flux density at the observations point with shield sh-1, and $B_{sh-2}$ is the magnetic flux density at the same point with shield sh-2.

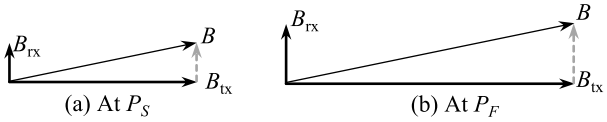


Fig. 8. Phasor diagram of the MFE (a) at $P_S$ and (b) at $P_F$ from the transmitter and receiver pads.

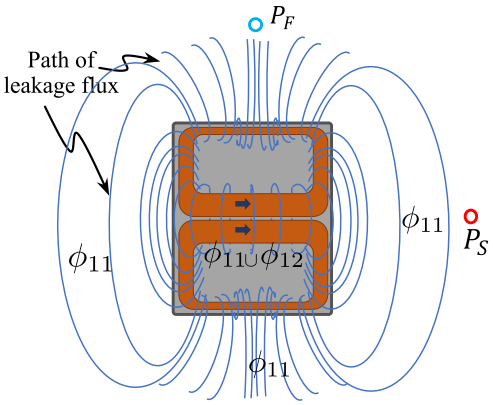


Fig. 9. Leakage flux from a single DD pad: $\phi_{11}$ indicates the self-flux that couples only between two windings of a pad, and $\phi_{12}$ indicates the mutual flux that couples with the receiver.

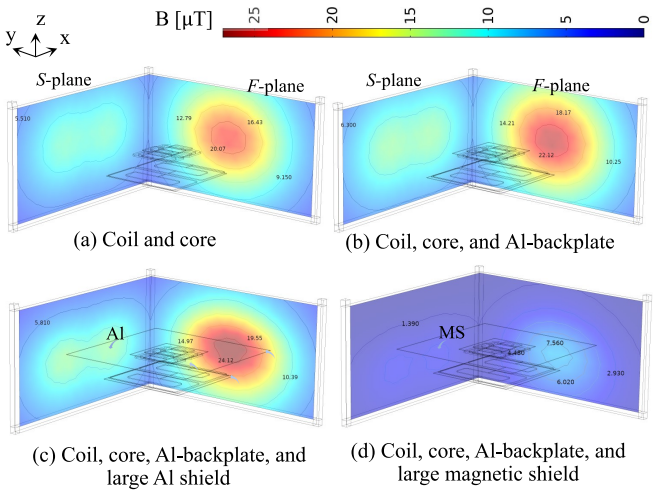


(a) Coil and core

(b) Coil, core, and Al-backplate

(c) Coil, core, Al-backplate, and large Al shield

(d) Coil, core, Al-backplate, and large magnetic shield

Fig. 10. MFE from an 11 kW DD-coil-based WCS under different shielding conditions.

Contrary to the MFE of the unipolar pad, the MFE of the bipolar pad has dominant $x$- and $y$-components [14]. Hence, the aluminum shield cannot effectively suppress the MFE of the bipolar pads. Rather, a high-permeability MS can be effective in shunting and suppressing the MFE of the bipolar pads. Three different pad configurations were simulated to evaluate the effectiveness of the aluminum and MS for the DD pads, and the results are shown in Fig. 10. The results in Fig. 10 (a) and (b) show that the addition of the aluminum backplate slightly increased the MFE compared to the design without any aluminum. The results in Fig. 10 (c) show that instead of suppressing the MFE, the large aluminum shield increased the MFE even more. On the other hand, a large MS above the receiver pad, as shown in Fig. 10 (d), significantly reduced the MFE of the DD coil-based WCS. Further results of different shield configurations for DD and unipolar coils under aligned and misaligned positions are published in [35].

Although the results with the MS are promising, the large shield shown in Fig. 10 (d) is not an optimized solution. In the next section, a detailed design and optimization method of

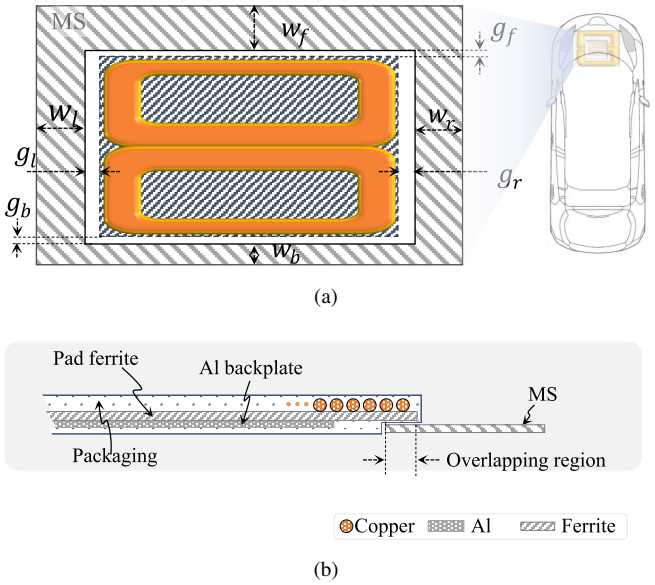


Fig. 11. (a) Illustrative sketch of the proposed MS geometry around a DD charging pad, and (b) the crossectional view of the coil, core, and shield.

Table III
DESIGN PARAMETERS OF THE PROPOSED MS

| Design parameter | Parameter symbol | Importance |
|---|---|---|
| Gap from core-ferrite | $g_l, g_r, g_f, g_b$ | High |
| Width of the MS | $w_l, w_r, w_f, w_b$ | Medium |
| Thickness of the MS | $t_l, t_r, t_f, t_b$ | Low |

the MS are presented to minimize the required shield material while suppressing the MFE.

## IV. PROPOSED MS

In this section, the design and optimization of the proposed MS are presented for an 11 kW DD-pad-based WCS. An illustrative sketch of the proposed MS is shown in Fig. 11 and the design parameters of the proposed MS are given in Table III. Although the figure shows a plate-type MS, based on the magnitude and direction of the magnetic flux in the MS, either a continuous layer or bar-type MS can be used. For the high flux–density region, a plate-type MS is the most suitable option, whereas, for the low flux–density region, a bar-type MS can minimize the overall cost and weight.

An FEA model of the proposed plate-type MS around a DD pad is shown in Fig. 12. For the lower power WCSs (<20 kW), either transmitter- or receiver-side MS is sufficient. For higher-power WCSs (>20 kW), both-side MS might be essential to suppress the MFE below the ICNIRP limit. In this case study of an 11 kW WCS, only the transmitter-side shield was used.

The parameters of the MS need to be designed depending on the required shielding effectiveness (SE) and power level. The width, thickness, and the gap of the MS around the pad determine the SE. Considering the EV charging, the required SE on the left and right are the same, requiring $w_r = w_l$ and $t_r = t_l$. The width and thickness along the front and back of the MS depend on the mounting position of the receiver. If the receiver is mounted near the front of the vehicle, the

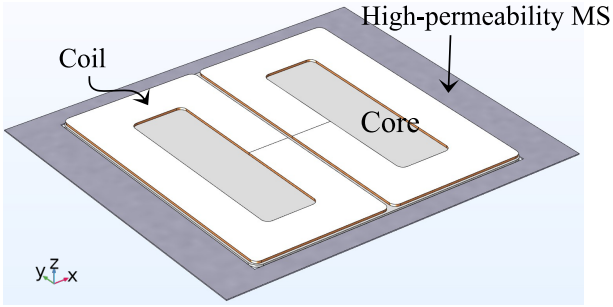


Fig. 12. FEA model of the proposed MS around a DD coil-based WCS pad.

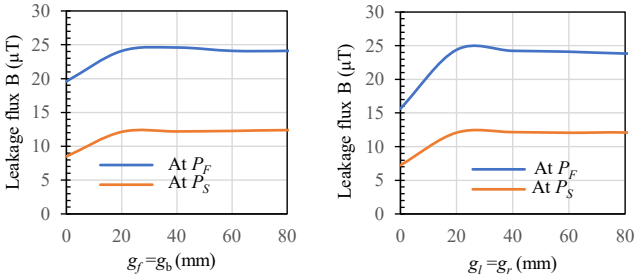


Fig. 13. Sensitivity of the MFE (a) with $g_f$ and $g_b$ (while $g_l = g_r = 50$ mm, $w_i = 100$ mm) and (b) with $g_l$ and $g_r$ (while $g_f = g_b = 50$ mm, $w_i = 100$ mm).

required SE for the front side will be higher than the backside and vice versa. In this paper, a generalized design is presented considering 800 mm clearance from the center of the receiver pad to the sides and front of the vehicle.

### A. Sensitivity of MFE to MS Parameters

The gap between the core and the MS ($g_f$, $g_b$, $g_l$, and $g_r$) critically affects the SE. The subscript $f$, $b$, $l$, and $r$ indicate the direction from the charging pad to the vehicle's front, back, left, and right, as shown in Fig. 11 (a).

*1) Gap between core and MS on the front and back, $g_f$, $g_b$:* The sensitivity of the MFE with respect to $g_f$ and $g_b$ is shown in Fig. 13 (a). The results show the high sensitivity of the MFE at the lower range of the gaps (0–20 mm). The results indicate that keeping the core continuously extended with $g_f = g_b \approx 0$ is crucial to achieving a high SE and suppressing the MFE. However, extending the main core outside the charging pad would be practically challenging. A separate MS layer can be extended keeping a certain overlapping region between the core and the MS, as shown in Fig. 11 (b). This approach allows the packaging of the MS within the same enclosure as the rest of the transmitter components. The primary target is to provide a low reluctance return path to the leakage flux of the pad.

*2) Gap between core and MS on the sides, $g_l$, $g_r$:* The sensitivity of the MFE with respect to $g_l$ and $g_r$ is shown in Fig. 13 (b). The figure shows a similar sensitivity characteristic indicating that placing a ferrite strip next to the core without any gap has the most significant impact on MFE reduction. The results in Fig. 13 (a) and (b) show that the sensitivity of the

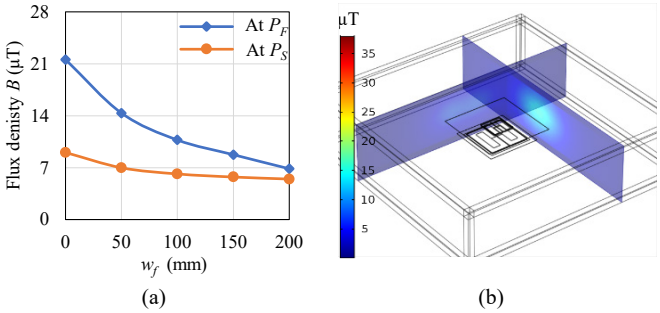


Fig. 14. Variation of the MFE at $P_F$ and $P_S$ with the varying shield width, $w_f$, while $w_b, w_r, w_l$ were kept fixed at 50 mm and $g_x = g_y = 0$ mm, (b) MFE on the F-plane and S-plane for $w = 100$ mm on all sides of the MS.

MFE with $g_l$, $g_r$ is comparatively higher than the sensitivity with $g_f$, $g_b$. These findings conclude that the core and MS layers must be adjacent to the core-ferrite with a minimum gap or a certain overlapping region.

*3) Width and thickness of the MS:* The width and thickness of the MS determine the SE and the shield loss. Fig. 14 (a) shows that with a 100 mm wide ferrite around the transmitter pad, the MFE was reduced to 10.6 $\mu T_{RMS}$, compared to 22 $\mu T_{RMS}$ without any shield. Considering the 27 $\mu T_{RMS}$ limit of ICNIRP, this shield is highly effective. As the MFE increases with the misalignment, the MFE must be kept much below the safety limit at the aligned condition. Fig. 14 (b) shows the flux density on the S-plane and F-plane for an MS width of $w = 100$ mm along all sides.

The width of the shield needs to be increased to achieve an even higher SE. The shielding requirements along the front, back, left, and right sides depend on the installation location of the WCS. The MFE for the DD pads is approximately twice around the front and back of the pad compared to the sides, which makes the shield design challenging if the front clearance is about the same as the sides.

*4) Transmitter vs Receiver side MS:* The MS can be applied both on the transmitter and receiver sides. Either a transmitter or a receiver side MS can provide limited shielding effectiveness. While a single-sided MS can be sufficient for an 11 kW WCS, a double-sided MS will be required for a higher power WCS [36]. As the MS includes additional material and cost to the charging pad and increases its effective size, a transmitter side MS is preferred. The transmitter has a comparatively less stringent limit on size and weight. Moreover, the utilization of a transmitter on a charging station is typically much higher than the receiver. Therefore, a transmitter side shield is highly preferred. However, for high-power WCSs and for better interoperability, both transmitter and receiver side MS will be required [35]. In this study, the design and test of a transmitter-side MS are shown for an 11 kW system; and a similar approach can be applied for the receiver-side MS design.

## B. MS Materials

The MS needs to provide a low-reluctance and low-loss path for the magnetic flux. In addition, the weight and volume of the MS should be minimized. Ferrite, nanocrystalline, and magment are the most promising magnetic materials for MS. The relative permeability of the low-frequency (<500 kHz) ferrites and nanocrystalline ranges from 500 to 6000, and 100 to 150000, respectively. The relative permeability of the magment is only 40. While those materials show a widely different relative permeability, most of those are found highly effective for shield designs.

Ferrite tiles are currently the most prominent materials for the MS. However, ferrites are highly brittle, which makes it challenging to build a shield with ferrites for EV application. Magment is a promising MS material, especially for the transmitter side [39]. Since Magment can be cast into the desired geometry, it is convenient for installing within the pavement of the parking area. Although Magment and ferrites are suitable for the transmitter side, nanocrystalline materials are another potential material for the receiver MS. Using multiple layers of narrow nanocrystalline ribbons, a flexible and thin layer of MS can be designed. For the nanocrystalline, the eddy current path must be controlled by a geometric modification to limit the loss [40].

## C. Optimization of the Proposed MS

The shield needs to be designed to suppress the MFE below a certain safety limit. Designing for excessive SE will require a higher weight and volume of shield material and increase the cost and design complexity. Moreover, the proposed MS includes additional weight, and it impacts the overall efficiency, either positively or negatively, based on the design. Therefore, considering all these goals and constraints, a multi-objective optimization function is proposed to suppress the MFE to a certain threshold, adding the least amount of additional loss and material as follows:

$$\Phi = \begin{cases} c_1(\frac{B_{P_S}}{B_{th1}} - 1) + \\ c_2(\frac{B_{P_F}}{B_{th2}} - 1) + \\ c_3(\frac{B_{MS}}{B_{th3}} - 1) \end{cases} \tag{12}$$

where $\Phi$ is the set of cost functions for minimization, $B_{th1}$, $B_{th2}$, and $B_{th3}$ are the target values, and $c_1$, $c_2$, and $c_3$ are the weights of the maximum flux density at $P_F$, $P_S$, and in the MS, respectively. Table III shows the parameters to be optimized.

The threshold flux densities in (12) are determined by the design constraints of the MFE and the MS material. The limits $B_{th1}$ and $B_{th2}$ are determined by the MFE limits under consideration and the worst-case operating condition. According to the ICNIRP 2010 guideline, the general public limit of the MFE is 27 $\mu T_{RMS}$, and it is 15 $\mu T_{RMS}$ for people carrying medical implant devices such as pacemakers. In this study, mostly the 27 $\mu T_{RMS}$ limit is considered in general, and a stricter limit of 15 $\mu T_{RMS}$ is chosen as the threshold to keep a certain buffer considering various uncertainties of operating conditions. A lower threshold value needs to be chosen to design for the 15 $\mu T_{RMS}$ limit of the pacemaker.

The choice of $B_{th3}$ is determined by the MS material and the operating frequency and temperature limit imposed on the MS. In this study, FR438081IC core is used as MS.

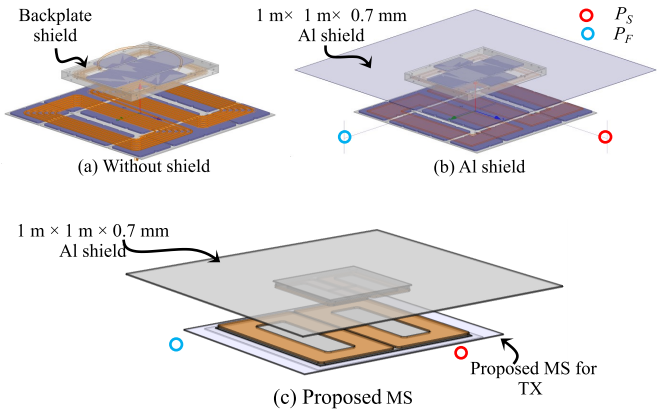


Fig. 15. FEA models of three WCS configurations: (a) basic transmitter and Receiver with the coil, core, and backplate, (b) an Aluminum shield is added above the receiver, and (c) the proposed MS added around the transmitter pad.

At 85 kHz, 150 mT provides sufficiently low loss density to keep the temperature below 80°C. To design a thinner MS, a higher threshold of $B_{th3}$ (up to 250 mT) can be set considering the advanced thermal design/packaging. Again, for a comparatively low-frequency operation, such as 20 kHz or 40 kHz, $B_{th3}$ can be higher up to 400 mT.

The choice of relative weight indicates the design priority and how strict the limits are for the thresholds $B_{th1}$, $B_{th2}$, and $B_{th3}$. In this system, suppressing the MFE to the given limit is of much high priority than the loss in the MS. Based on these considerations and the operating condition, in this study, the optimization is performed through FEA with $c_1 = c_2 = 0.4, c_3 = 0.2$, $B_{th1} = B_{th1} = 15$ $\mu T_{RMS}$, and $B_{th3} = 150$ $mT_{peak}$.

### *D. FEA of the Proposed MS*

The effectiveness of the proposed shield is investigated for an 11 kW mismatched DD-coil WCS. The design parameters of the system are given in Table IV. In this system, the receiver length and width are approximately half of the transmitter. The three different shield configurations evaluated with the 11 kW system are shown in Fig. 15. Three different WCS configurations are the basic WCS, which consists of the basic transmitter and receiver coil with core and aluminum backplate; the aluminum shield, which is a large aluminum plate placed above the receiver pad of the basic WCS; and the MS, which is the proposed MS. For each of the configurations, the MFE was observed at both $P_F$ and $P_S$.

For the three configurations shown in Fig. 15, SEs are obtained from FEA simulations and presented in Table IV. Compared to the basic WCS, the SE of the Al shield is higher than one, indicating that, instead of suppressing, the Al shield increases the MFE. Compared to the aluminum shield, the proposed MS shows a SE=0.3 both in the front and side of the vehicle. The proposed shield can be further optimized to reduce the MFE to meet the lower MFE limits. These results indicate that the Al shield increases the field emissions by 16% and 4% at the frontal and lateral observation points. However, the proposed MS reduces the field emissions by 70% on both the frontal and lateral observation points.

Table IV
FEA–BASED COMPARISON OF SE

| Shield Configurations | Relative SE | SE at $P_F$ | SE at $P_S$ |
|---|---|---|---|
| Al shield: Fig. 15 (b) | $_{\text{Basic-WCS}}SE_{\text{Al-Sh}}$ | 1.16 | 1.04 |
| Proposed shield: Fig. 15 (c) | $_{\text{Al-Sh}}SE_{\text{MS}}$ | 0.30 | 0.30 |

Table V
INDUCTANCE AT ALIGNED AND MISALIGNED POSITIONS

| Shield configurations | Aligned | | | Misaligned | | |
|---|---|---|---|---|---|---|
| | $L_{tx}$ (μH) | $L_{rx}$ (μH) | $M$ (μH) | $L_{tx}$ (μH) | $L_{rx}$ (μH) | $M$ (μH) |
| Basic WCS | 82.3 | 85.5 | 18.6 | 80.5 | 85.5 | 13.5 |
| +Large Rx Al shield | 80.3 | 85.2 | 19.4 | 77.8 | 85.1 | 14.2 |
| +Proposed Tx MS | 81.9 | 85.2 | 19.3 | 79.4 | 85.2 | 14.1 |

The inductance of the primary and secondary coils changes with different shield configurations and alignment conditions. The self and mutual inductance under the aligned and maximum misaligned conditions are given in Table V. The variation in inductance changes the resonance frequency and the current gain of the system. In this study, the operating frequency was kept fixed at 85 kHz and only the currents through the coils were increased to transfer 11 kW output power under the maximum misaligned position.

## V. EXPERIMENTAL RESULTS

The experimental setup of an 11 kW EV WCS is shown in Fig. 16. The transmitter and receiver pads are mismatch coils with different dimensions and number of turns. The receiver coils of the EV WCSs are typically designed smaller than the transmitter coils in order to achieve higher misalignment tolerance and to have a smaller and lightweight coupler on the vehicle side. The transmitter and receiver pad of the prototype system have 6.25 and 8.25 turns, respectively. Both the transmitter and receiver pad are series compensated. The WCS configurations and the measured parameters are given in Table VI.

The proposed MS is formed by using strips of 100 mm wide and 3.8 mm thick ferrite core (FR438081IC) around the transmitter pad. The experimental setup with the SAE recommended large Al shield is shown in Fig. 16 (a). In SAE J2954, the area of the Al shield of a charging pad mounted under an EV is (800×800) mm. However, for the laboratory test stand, the recommended shield consists of a (1.1×1.1)

Table VI
DESIGN PARAMETER OF 11–KW WCS

| Parameter | Transmitter | Receiver |
|---|---|---|
| Power rating | 11 kW | |
| Airgap | 150 mm | |
| Compensation type | Series-Series | |
| Size of the pad | (650×650) mm | (350×350) mm |
| Ferrite core thickness | 5 mm | 5 mm |
| Number of turns | 6.25 | 8.2 |
| Inductance | 78 μH | 89 μH |
| Coil current (RMS) | 41.3 A | 39.8 A |

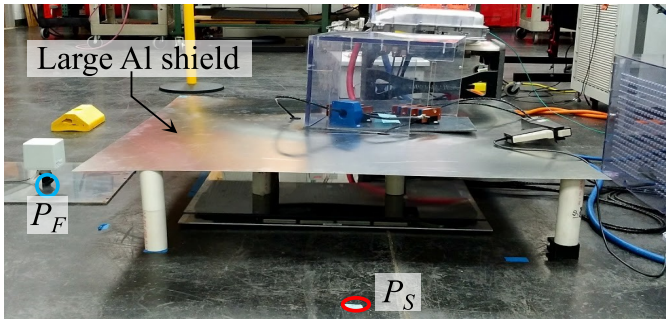


(a) WCS with the large aluminum shield

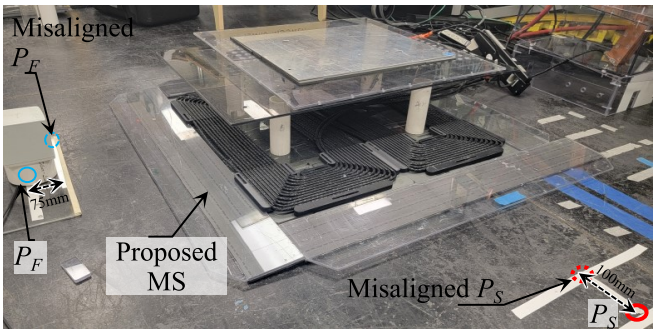


(b) WCS with the proposed MS

Fig. 16. Wireless charging systems with (a) the large aluminum shield above the receiver pad and (b) the proposed MS around the transmitter pad.

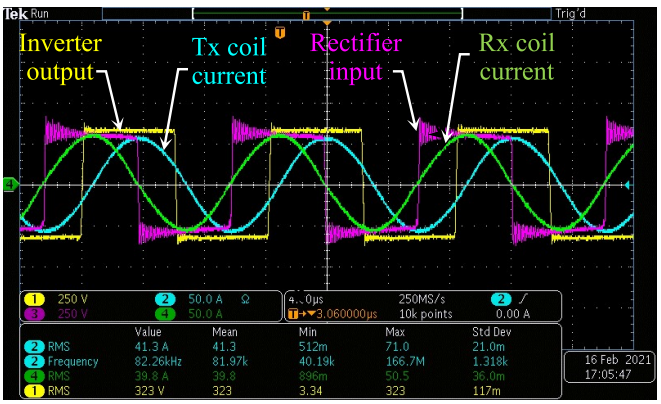


Fig. 17. The transmitter and receiver coil currents of the 11 kW WCS with 94.8% dc-to-dc efficiency at the rated output power.

m Al plate and a (1.5×1.5) m steel plate, which mimics the shield and EV undercarriage, respectively. In this study, only a large (1 ×1) m aluminum shield is used above the receiver pad to approximately mimic the EV undercarriage since the large aluminum shield already magnetically isolates the EV undercarriage to a great extent. The proposed MS is shown in Fig. 16 (b).

The SE of the aluminum shield and the proposed MS were evaluated by measuring the frequency spectrum of the stray magnetic field at the proposed observation points using a Narda EHP-200A isotropic EMF analyzer. The magnetic field was observed at $P_F$ and $P_S$, and the sensor was placed such that the center of the probe was aligned with the observation point. The position of the probe was moved with the receiver

Table VII
EXPERIMENTAL MFE UNDER ALIGNED POSITION

| Shield configurations | $I_{Tx}$ ($A_{RMS}$) | $I_{Rx}$ ($A_{RMS}$) | $B_{RMS}$ at $P_F$ (μT) | $B_{RMS}$ at $P_S$ (μT) | $P_{out}$ (kW) |
|---|---|---|---|---|---|
| Basic WCS | 39.1 | 41.1 | 19.08 | 12.28 | 11.0 |
| +Large Al shield | 39.3 | 41.1 | 24.89 | 12.29 | 11.0 |
| +Proposed MS | 39.8 | 41.3 | 9.84 | 5.89 | 11.0 |

pad while testing the MFE under the misaligned conditions to maintain the same relative position to the center of the receiver.

The resulting transmitter and receiver coil currents under aligned conditions were 41.3 A and 39.8 A, respectively. The waveforms of currents in the coils and the output voltage of the inverter are shown in Fig. 17. The DC-to-DC efficiency of the system was found approximately 94.8% at rated 11 kW output power.

At 11 kW output power, the MFEs for the different shield configurations under aligned conditions are summarized in Table VII. The transmitter and receiver currents in this test results are nearly sinusoidal, as shown in Fig. 17; therefore, the third and fifth harmonic components of the spectra are also small. Depending on tuning topology and operating frequency, the third harmonic component can be significant and needs to be considered accordingly.

The intrinsic MFE of the system without any additional shield was 19.08 $\mu T_{RMS}$ at $P_F$ and 12.28 $\mu T_{RMS}$ at $P_S$ as shown in Fig. 18 (a) and (b), respectively. When the large aluminum shield was added, the field density at $P_F$ increased to 24.89 $\mu T_{RMS}$, whereas the MFE at $P_S$ remained about the same as shown in Fig. 18 (c) and (d), respectively. The large aluminum shield increased the MFE more on the F-plane than on the S-plane. On the other hand, the proposed MS effectively reduced the MFE to 9.8 $\mu T_{RMS}$ and 5.9 $\mu T_{RMS}$ at $P_F$ and $P_S$, respectively, as shown in Fig. 18 (e) and (f). Using the proposed MS, the MFE can be reduced below both the ICNIPR general-public limit of 27 $\mu T_{RMS}$ and pacemaker limit of 15 $\mu T_{RMS}$.

The results show that the MFE with a traditional large aluminum shield was close to the ICNIRP 2010 general-public exposure limit even for the aligned position of the transmitter and receiver. Any misalignment would make the system vulnerable to exceeding the ICNIRP limits. The proposed MS suppressed the MFE by 50.5% compared to the aluminum shield, and much below the ICNIPR limit.

The MFE significantly increases under a misaligned position as the observation points get closer to the transmitter pad while maintaining the same distance for the center of the vehicle-side coupler. Moreover, it requires higher coil currents to transmit the same rated power due to the reduced mutual inductance under misalignment. The SAE J2954 requires ±100 mm maximum misalignment along the sides of the vehicle and ±75 mm along the length of the vehicle. In this study, the MFE is evaluated under the worst case of maximum misaligned position of the receiver with $\Delta x$=75 mm and $\Delta y$=100 mm. The observation points are measured relative to the vehicle pad; therefore, the new observation points under the misaligned position were also shifted accordingly, which

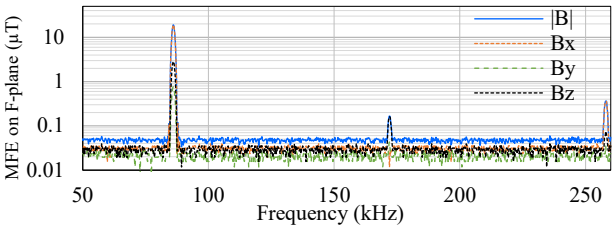


(a) MFE on the *F*-plane with backplate Al shield.

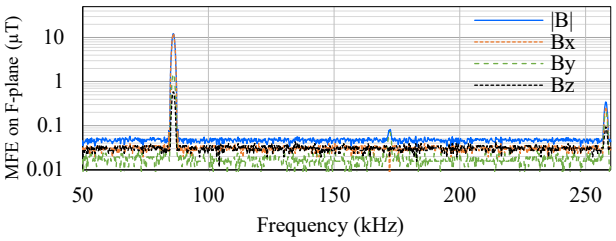


(b) MFE on the *S*-plane with backplate Al shield.

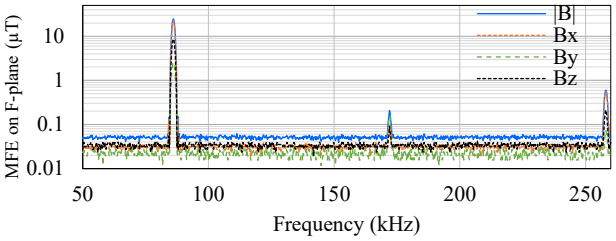


(c) MFE on the *F*-plane with large Al shield.

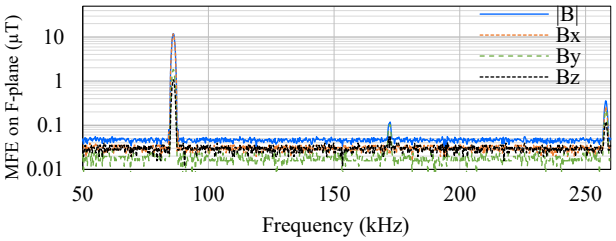


(d) MFE on the *S*-plane with large Al shield.

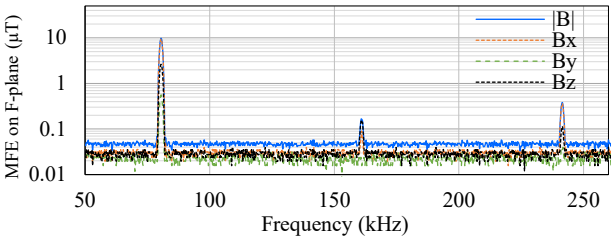


(e) MFE on the *F*-plane with proposed shield.

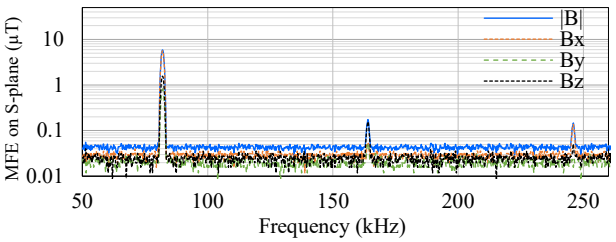


(f) MFE on the *S*-plane with proposed shield.

Fig. 18. Magnetic flux density spectrum with (a)-(b) Al backplate only, (c)-(d) with large Al shield, and (e)-(f) with the proposed MS at $P_S$ and $P_F$.

Table VIII
MFE UNDER MISALIGNED POSITIONS AT THE SAME TRANSMITTER CURRENT AS ALIGNED POSITION (41.1 $A_{RMS}$)

| Shield configurations | $I_{Tx}$ ($A_{RMS}$) | $I_{Rx}$ ($A_{RMS}$) | $B_{rms}$ at $P_F$ (μT) | $B_{rms}$ at $P_S$ (μT) | $P_{out}$ (kW) |
|---|---|---|---|---|---|
| Basic WCS | 41.1 | 25.4 | 26.4 | 16.0 | 5.3 |
| +Large Rx Al shield | 41.1 | 26.7 | 51.7 | 16.8 | 5.5 |
| +Proposed Tx MS | 41.1 | 27.3 | 28.0 | 10.5 | 5.6 |

Table IX
MFE UNDER THE MISALIGNED POSITIONS AT THE RATED 11 KW OUTPUT POWER

| Shield configurations | $I_{Tx}$ ($A_{RMS}$) | $I_{Rx}$ ($A_{RMS}$) | $B_{RMS}$ at $P_F$ (μT) | $B_{RMS}$ at $P_S$ (μT) | $P_{out}$ (kW) |
|---|---|---|---|---|---|
| Basic WCS | 59.3 | 37.8 | 37.6 | 23.8 | 11.0 |
| +Large Rx Al shield | 58.2 | 37.7 | 55.0 | 27.01 | 11.0 |
| +Proposed Tx MS | 58.4 | 38.1 | 39.1 | 14.5 | 11.0 |

came closer than 800 mm from the center of the transmitter pad.

The MFE under misaligned positions were measured at two different output power levels: first, at reduced power with the transmitter current about the same as the nominal current at the aligned position; second, at an increased transmitter current to transfer the rated 11 kW output power.

*1) MFE under misaligned condition with transmitter current same as aligned condition:* Table VIII shows the MFE results under misalignment with transmitter current 41.1 A when the output power was about 5.5 kW. The results of Table VIII show the significance of the reduced distance of the observation points from the transmitter under misalignment. Even the receiver currents are reduced by 30% compared to the aligned (11 kW) position, the MFE has been increased to approximately twice although the output power went down to 5.5 kW. At this power level, the MFE with the traditional Al is about 51.7 $\mu T_{RMS}$ at the observation point at the front of the vehicle and 16.8 $\mu T_{RMS}$ at the side of the vehicle. The results signify that if a WCS is installed at the front of the vehicle, it will be highly vulnerable to exceeding the ICNIRP limit under misaligned conditions. Even with the proposed MS the MFE is 28 $\mu T_{RMS}$ at $P_F$.

*2) MFE under misaligned condition at 11 kW output power:* Table IX shows the MFE results under maximum misalignment and at rated 11 kW output power. The efficiency of the system was reduced to 91.8%, compared to 94.8% at the aligned position. The coil currents were increased by about 1.45 times compared to Table VIII, hence, the MFE was also increased by about 1.4 to 1.5 times. At this power, the MFE with Al shield exceeds the ICNIRP general-public limit of 27 $\mu T_{RMS}$ both at $P_F$ and $P_S$. The proposed MS meets the ICNIRP limit of 15 $\mu T_{RMS}$ at $P_S$, however, exceeds the ICNIRP general-public limit at $P_S$. The results of the proposed MS at 11 kW output power and maximum misalignment are shown in Fig. 19.

From an optimization perspective, the MS is not further optimized as the position of $P_F$ will vary depending on the installation location of the receiver pad relative to the front

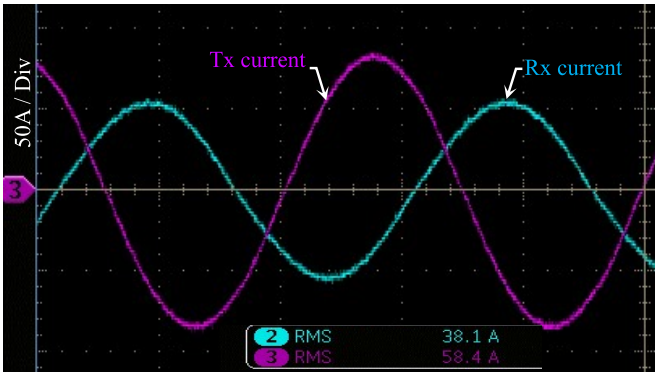


(a) Coil currents under misaligned position

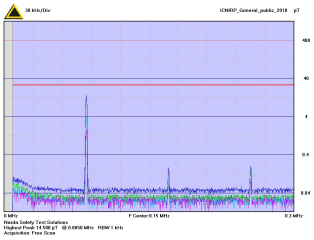

(b) MFE at $P_S$

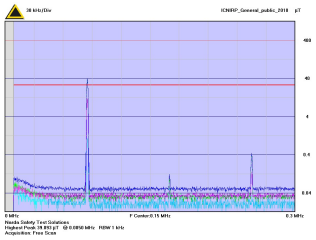

(c) MFE at $P_F$

Fig. 19. Experimental results under misaligned position with the proposed MS: (a) transmitter and receiver coil currents, (b) MFE at $P_S$, and (c) MFE at $P_F$.

bumper of the vehicle. Further experimental results show that with an additional 100 mm clearance (900 mm from the center of the receiver), the proposed MS meets the ICNIRP general-public limits under all conditions. If such clearance is not achievable for a certain vehicle class, then a larger MS can be designed to suppress the MFE under misaligned conditions, as shown in previous publications [14], [35]. Furthermore, for higher power bipolar coil-based WCSs, the MFE will increase even more. The proposed MS can be effectively applied by optimizing the design parameters following the proposed algorithm to meet the safety limits.

## VI. Conclusions

In this paper, the MFE characteristics of a high-power WCS with DD coils were investigated. A novel magnetic shielding technique with an optimization process was proposed to suppress the MFE below the ICNIRP 2010 limit of 27 $\mu T_{RMS}$. In contrary to unipolar circular and rectangular pads, passive eddy current shielding of DD coils increased the MFEs. The magnetic field vectors of the DD coil showed a dominant XY-planar component at the observation points, compared with dominant Z-components in unipolar coils. A high-permeability ferrite-based magnetic shielding technique following the magnetic field pattern of the DD coil was developed to guide the leakage flux through a low reluctance path and limit the MFE. FEA of the proposed MS showed suppression of the MFE for an 11 kW system from 24.89 to 9.84 $\mu T_{RMS}$ at the front and from 12.29 to 5.89 $\mu T_{RMS}$ at the sides of the vehicle. Extensive experimental validation of the proposed shielding technique for an 11 kW mismatched DD-coil WCS showed an effective reduction of the MFE below the ICNIRP limit. The proposed MS can be extended and applied to suppress MFE from extremely high-power DD and bipolar coil-based WCSs.

## VII. Acknowledgment

This research used the resources available at the Power Electronics and Electric Machinery Laboratory at the National Transportation Research Center, a US Department of Energy (DOE) Office of Energy Efficiency and Renewable Energy user facility operated by the Oak Ridge National Laboratory (ORNL). The authors would like to thank Dr. Burak Ozpineci (ORNL) for his managerial support and technical guidance and Lee Slezak (DOE) for funding this work and project guidance.

## References

[1] P. Machura and Q. Li, "A critical review on wireless charging for electric vehicles," *Renewable and Sustainable Energy Reviews*, vol. 104, pp. 209–234, 2019.

[2] A. Foote and O. C. Onar, "A review of high-power wireless power transfer," in *IEEE Transportation Electrification Conference and Expo (ITEC)*, 2017.

[3] D. Patil, M. K. McDonough, J. M. Miller, B. Fahimi, and P. T. Balsara, "Wireless power transfer for vehicular applications: Overview and challenges," *IEEE Transactions on Transportation Electrification*, vol. 4, no. 1, pp. 3–37, 2017.

[4] G. A. Keoleian, Z. Bi, Y. Zhang, Z. Zhao, T. Kan, and C. C. Mi, "A review of wireless power transfer for electric vehicles: Prospects to enhance sustainable mobility," *Applied Energy*, vol. 179, pp. 413–425, 2016.

[5] C. C. Mi, G. Buja, S. Y. Choi, and C. T. Rim, "Modern advances in wireless power transfer systems for roadway powered electric vehicles," *IEEE Transactions on Industrial Electronics*, vol. 63, no. 10, pp. 6533–6545, 2016.

[6] G. A. Covic and J. T. Boys, "Modern trends in inductive power transfer for transportation applications," *IEEE Journal of Emerging and Selected Topics in Power Electronics*, vol. 1, no. 1, pp. 28–41, 2013.

[7] SBWire Report. (2020) Dynamic wireless EV charging system market to witness huge growth by 2025: Robert Bosch, Continental, Toyota Motor, Toshiba. [Online]. Available: http://www.sbwire.com/

[8] EVADOPTION. (2020) EV market share. [Online]. Available: https://evadoption.com/ev-market-share/

[9] M. Mohammad, J. Pries, O. Onar, V. P. Galigekere, G.-j. Su, S. Anwar, J. Wilkins, and D. Utkarsh, "Design of an EMF suppressing magnetic shield for a 100-kW DD-coil wireless charging system for electric vehicles," in *IEEE Applied Power Electronics Conference and Exposition (APEC)*, 2019.

[10] Y. Yashima, H. Omori, T. Morizane, N. Kimura, and M. Nakaoka, "Leakage magnetic field reduction from wireless power transfer system embedding new eddy current-based shielding method," in *International Conference on Electrical Drives and Power Electronics (EDPE)*, 2015.

[11] A. A. S. Mohamed, A. Meintz, P. Schrafel, and A. Calabro, "In-vehicle assessment of human exposure to EMFs from 25-kW WPT system based on near-field analysis," in *IEEE Vehicle Power and Propulsion Conference (VPPC)*, 2018.

[12] T. Campi, S. Cruciani, M. Feliziani, and F. Maradei, "Magnetic field generated by a 22 kW-85 kHz wireless power transfer system for an EV," in *AEIT International Annual Conference*, 2017.

[13] P. P. Ding, L. Bernard, L. Pichon, and A. Razek, "Evaluation of electromagnetic fields in human body exposed to wireless inductive charging system," *IEEE Transactions on Magnetics*, vol. 50, no. 2, 2014.

[14] M. Mohammad, J. L. Pries, O. C. Onar, V. P. Galigekere, G. J. Su, and J. Wilkins, "Comparison of magnetic field emission from unipolar and bipolar coil-based wireless charging systems," in *IEEE Transportation Electrification Conference and Expo (ITEC)*, 2020, Conference Proceedings.

[15] S. Kim, H. H. Park, J. J. Kim, J. J. Kim, and S. Ahn, "Design and analysis of a resonant reactive shield for a wireless power electric vehicle," *IEEE Transactions on Microwave Theory and Techniques*, vol. 62, no. 4, pp. 1057–1066, 2014.

[16] S. Y. Choi, B. W. Gu, S. W. Lee, W. Y. Lee, J. Huh, and C. T. Rim, "Generalized active EMF cancel methods for wireless electric vehicles," *IEEE Transactions on Power Electronics*, vol. 29, no. 11, pp. 5770–5783, 2014.
[17] A. Tejeda, C. Carretero, J. T. Boys, and G. A. Covic, "Ferrite-less circular pad with controlled flux cancelation for EV wireless charging," *IEEE Transactions on Power Electronics*, vol. 32, no. 11, pp. 8349–8359, 2017.
[18] E. Asa, M. Mohammad, O. C. Onar, J. Pries, V. Galigekere, and G.-J. Su, "Review of safety and exposure limits of electromagnetic fields (emf) in wireless electric vehicle charging (wevc) applications," in *IEEE Transportation Electrification Conference & Expo (ITEC)*, 2020.
[19] SAE-J2954, "Wireless power transfer for light-duty plug-in/electric vehicles and alignment methodology J2954_202010," *Health Physics*, 2020.
[20] T. I. C. on Non-Ionizing Radiation Protection, "ICNIRP guideline for limiting exposure to time-varying electric and magnetic fields (1Hz-100kHz)," *Health Physics*, vol. 99, no. 6, pp. 818–836, 2010.
[21] E. S. Lee, Y. H. Sohn, B. G. Choi, S. H. Han, and C. T. Rim, "A modularized IPT with magnetic shielding for a wide-range ubiquitous Wi-Power zone," *IEEE Transactions on Power Electronics*, vol. 33, no. 11, pp. 9669–9690, 2018.
[22] A. U. Ibrahim, W. Zhong, and M. D. Xu, "A 50-kW three-channel wireless power transfer system with low stray magnetic field," *IEEE Transactions on Power Electronics*, vol. 36, no. 9, pp. 9941–9954, 2021.
[23] B. G. Choi, Y.-H. Sohn, E. S. Lee, S. H. Han, H. R. Kim, and C. T. Rim, "Coreless transmitting coils with conductive magnetic shield for wide-range ubiquitous IPT," *IEEE Transactions on Power Electronics*, vol. 34, no. 3, pp. 2539–2552, 2019.
[24] J. Li, F. Yin, and L. Wang, "Transmission efficiency of different shielding structures in wireless power transfer systems for electric vehicles," *CSEE Journal of Power and Energy Systems*, vol. 7, no. 6, pp. 1247–1255, 2021.
[25] W. Songcen, W. Bin, W. Xiaokang, X. Chong, X. Jinxing, G. Weimei, and X. Jiaqi, "Electromagnetic shielding design for magnetic coupler of N-type dynamic electric vehicle wireless power transfer systems," in *22nd International Conference on Electrical Machines and Systems (ICEMS)*, 2019.
[26] A. U. Ibrahim, W. Zhong, and M. D. Xu, "A 50-kW three-channel wireless power transfer system with low stray magnetic field," *IEEE Transactions on Power Electronics*, vol. 36, no. 9, pp. 9941–9954, 2021.
[27] P. R. Bannister, "New theoretical expressions for predicting shielding effectiveness for the plane shield case," *IEEE Transactions on Electromagnetic Compatibility*, vol. EMC-10, no. 1, pp. 2–7, 1968.
[28] J. Schneider, R. Carlson, J. Sirota, R. Sutton, E. Taha, M. Kesler, K. Kamichi, I. Teerlinck, H. Abeta, Y. Minagawa, S. Yazaki, U. Yoon, K. Kawashima, S. Muskett, T. Bohn, S. Mathar, D. Mikat, J. Guag, S. Seidman, and R. Reitan, "Validation of wireless power transfer up to 11 kW based on SAE J2954 with bench and vehicle testing," *SAE Technical Paper*, 2019.
[29] M. Jo, Y. Sato, Y. Kaneko, and S. Abe, "Methods for reducing leakage electric field of a wireless power transfer system for electric vehicles," in *IEEE Energy Conversion Congress and Exposition (ECCE)*, 2014.
[30] R. Bosshard and J. W. Kolar, "Multi-objective optimization of 50 kW/85 kHz IPT system for public transport," *IEEE Journal of Emerging and Selected Topics in Power Electronics*, vol. 4, no. 4, pp. 1370–1382, 2016.
[31] M. Lu and K. Ngo, "Circuit models and fast optimization of Litz shield for inductive power transfer coils," *IEEE Transactions on Power Electronics*, vol. 34, no. 5, pp. 4678–4688, 2018.
[32] F. Y. Lin, G. A. Covic, and J. T. Boys, "Leakage flux control of mismatched IPT systems," *IEEE Transactions on Transportation Electrification*, vol. 3, no. 2, pp. 474–487, 2017.
[33] F. Y. Lin, A. Zaheer, M. Budhia, and G. A. Covic, "Reducing leakage flux in IPT systems by modifying pad ferrite structures," in *IEEE Energy Conversion Congress and Exposition (ECCE)*, 2014.
[34] K. Song, G. Yang, Y. Guo, Y. Lan, S. Dong, J. Jiang, and C. Zhu, "Design of DD coil with high misalignment tolerance and low EMF emissions for wireless electric vehicle charging systems," *IEEE Transactions on Power Electronics*, vol. 35, no. 9, pp. 9034–9045, 2020.
[35] M. Mohammad, O. C. Onar, J. L. Pries, V. P. Galigekere, G.-J. Su, and J. Wilkins, "Analysis of magnetic field emissions and shield requirements for interoperating high-power EV wireless charging system," in *IEEE Applied Power Electronics Conference and Exposition (APEC)*, 2021.
[36] M. Mohammad, J. L. Pries, O. C. Onar, V. P. Galigekere, and G. J. Su, "Shield design for 50 kW three-phase wireless charging system," in *IEEE Energy Conversion Congress and Exposition (ECCE)*, 2020.
[37] M. Mohammad, "Optimization of inductive wireless charging systems for electric vehicles: Minimizing magnetic losses and limiting electromagnetic field emissions," Thesis, The University of Akron, 2019.
[38] J. Pries, V. P. Galigekere, O. C. Onar, G.-J. Su, R. Wiles, L. Seiber, J. Wilkins, S. Anwar, and S. Zou, "Coil power density optimization and trade-off study for a 100 kW electric vehicle IPT wireless charging system," in *Energy Conversion Congress and Exposition (ECCE)*, 2018.
[39] MAGMENT. (2020) Magnetic cement MC40 material datasheet. [Online]. Available: https://www.magment.de/en-products/
[40] M. Xiong, X. Wei, Y. Huang, Z. Luo, and H. Dai, "Research on novel flexible high-saturation nanocrystalline cores for wireless charging systems of electric vehicles," *IEEE Transactions on Industrial Electronics*, vol. 68, no. 9, pp. 8310–8320, 2021.

**Mostak Mohammad** (S'15–M'19–SM'20) completed his B.Sc. degree in 2009 in electrical and electronics engineering from the Bangladesh University of Engineering and Technology (BUET), Bangladesh, and his Ph.D. in Electrical Engineering in 2019 from the University of Akron, OH, USA. From 2009 to 2014, he worked as a specialist in Radio Network Planning in Robi Axiata Limited, Bangladesh, where he developed RF propagation models for FEA-based cellular network design and optimization.

Dr. Mohammad is currently working as an R&D Staff in the National Transportation Research Center at Oak Ridge National Laboratory. He has been working on 11 kW to 300 kW single-phase, poly-phase, stationary and dynamic wireless charging systems. His research interests include high-fidelity multi-physics modeling and optimization, high-power wireless charging for electric vehicles, magnetic design, electromagnetic shielding, electric machine design and optimization, and additive-manufactured magnetic materials.

**Omer C. Onar** (S'05–M'10–SM'18) received his Ph.D. degree from Illinois Institute of Technology (IIT) in Electrical Engineering, in July 2010, Chicago, IL.

In July 2010, he received the Alvin M. Weinberg Fellowship at the U.S. Department of Energy's Oak Ridge National Laboratory, where he joined the Power Electronics and Electric Machinery Group. At Oak Ridge National Laboratory, he has worked on advanced power electronics and electric drives, renewable energy, energy storage systems, and wireless power transfer systems. He is currently leading the Vehicle Power Electronics Research Group at the Oak Ridge National Laboratory. He is an Associate Editor for the IEEE Transactions on Transportation Electrification and the IEEE Transactions on Power Electronics.

Dr. Onar is the recipient of a U.S. Department of Energy Vehicle Technologies Office Distinguished Achievement Team Award and a UT-Battelle Research Accomplishment Team Award for his work on wireless power transfer systems in 2016. He also received an R&D 100 Award jointly with Toyota TEMA for wireless charging of EVs.

**Veda Prakash Galigekere** (GS'9—M'12—SM'19) was born in Bangalore, India, in 1982. He received his B.E. degree in Electrical Engineering from Visvesvaraya Technological University, Bangalore, India, in 2004. He received his M.S. and Ph.D. degrees in Electrical Engineering from Wright State University, Dayton, Ohio, USA, in 2007 and 2012, respectively.

In 2008 and 2012 he was an Intern at General Electric Global Research Center in Bangalore, India. From 2012 to 2016 he was with Lear Corporation, Southfield, MI, USA. He is currently a research and development staff member at the Power Electronics and Electric Machinery Group, Oak Ridge National Laboratory, TN, USA. His research interests include high-power wireless power transfer, high-frequency resonant converters, impedance source converters, and small-signal modeling and control of PWM dc-dc converters.

Dr. Galigekere has served as Guest Associate Editor for the IEEE Transactions on Power Electronics and is currently an Associate Editor for the IEEE Transactions on Industry Applications.

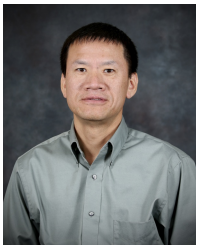

**Gui-Jia Su** received the B.S., M.S., and Ph.D. degrees in 1985, 1989, and 1992, respectively, all in Electrical Engineering.

From 1992 to 1995, he was an assistant professor at Nagaoka University of Technology, Japan. From 1995 to 1998, he was with Sanken Electrical Co., Ltd., Japan, where he engaged in research and development of uninterruptible power supplies, sensorless PM motor drives, and power factor correction for single- and three-phase rectifiers. In 1998, he started working at the Power Electronics and Electric Machinery Research Center at the Oak Ridge National Laboratory as a research scientist and is currently a distinguished member of the R&D staff. His research interests include DC/DC converters, inverters, wired and wireless battery chargers, and traction motor drives for electric vehicle applications.

Dr. Su is a Battelle Distinguished Inventor and received the U.S. Department of Energy Vehicle Technologies Office Distinguished Achievement Award in 2019.

**Jonathan Wilkins** received his B.Sc. in Physics and B.Sc. in Mathematics from the Bethany College in West Virginia in 2002. He also received his Associate degree in Industrial Engineering Technologies and Mechanical Engineering Technologies from the Pellissippi State Technical College in 2017 and 2018, respectively. He is currently a technical professional at the Vehicle Power Electronics Research Group at the Oak Ridge National Laboratory. His focus areas include wireless and plug-in electric vehicle charging systems, power electronic converters, inverters, compact electric motors, and experimental test setup instrumentation and apparatus.